MASTERARBEIT | MASTER'S THESIS

Titel | Title

Characterisation of synthetic star corundum

verfasst von | submitted by

Juliana Einzmann

angestrebter akademischer Grad | in partial fulfilment of the requirements for the degree of

Master of Science (MSc)

Wien | Vienna, 2025

Studienkennzahl lt. Studienblatt | Degree programme code as it appears on the student record sheet:	UA 066 815
Studienrichtung lt. Studienblatt | Degree programme as it appears on the student record sheet:	Masterstudium Erdwissenschaften
Betreut von | Supervisor:	Univ.-Prof. Dr. Lutz Nasdala

Acknowledgements

First and foremost, I would like to express my sincere gratitude to Prof. Dr Lutz Nasdala for supervising my M.Sc. and for his continuous guidance throughout the course of this work. I am also grateful to Prof. Dr Manfred Wildner, Prof. Dr Christoph Hauzenberger (Univ. Graz), Prof. Dr Gerald Giester, and Franz Kiraly for their valuable advice and their contributions to the analytical work. My thanks further go to Andreas Wagner (all Univ. Wien) for the careful sample preparation, as well as Rangsithat Rungserichai (Aue Gems Co., Ltd) and Dr Bhuwadol Wanthanachaisaeng (GIT Bangkok) for kindly providing the samples used in this study.

Special thanks are also due to Jamie Newman and Andrea Mason, American Museum of Natural History, New York, for providing a photograph of the 'Star of India' sapphire, and to the Board of the Museum for granting permission to present this image herein. Finally, I would like to express my heartfelt gratitude to my friends and family for their constant encouragement, patience, and emotional support during the preparation of this thesis.

Acknowledgement of the usage of AI

I acknowledge having used the AI tool *ChatGPT* (https://chatgpt.com/) to support the refinement of academic wording and to suggest stylistic improvements. I confirm that I am familiar with the University of Vienna's guidelines on AI usage and that this thesis is in full accordance with them.

Table of Contents

ABSTRACT (GERMAN)

Diese Arbeit präsentiert die Ergebnisse einer mineralogischen Charakterisierung von synthetischem Sternkorund (gelber Saphir, blauer Saphir und Rubin), hergestellt durch Verneuil-Synthese mit anschließender Ti-Diffusion. Alle untersuchten Cabochons zeigen einen deutlich ausgeprägten sechsstrahligen Stern, der durch Rutilnadeln in der Diffusionszone hervorgerufen wird. Der blaue Saphir weist einen intensiven Diffusionsrand mit hohen Fe-Gehalten (8260 ± 290 ppm) auf, während das Kernmaterial farblos bleibt. Der Rubin enthält erhöhte Cr-Konzentrationen (3780 ± 150 ppm), die seine rote Farbe erklären, wohingegen der gelbe Saphir durch Mg-Fe-Trapped-Hole-Zentren gefärbt ist. In allen Proben wurden ungewöhnlich hohe Si-Gehalte (3730 ± 200 bis 4090 ± 200 ppm) nachgewiesen, deren Ursprung bislang ungeklärt ist. Raman-spektroskopische Analysen zeigen im Kristallinneren typische Korund-Spektren, an den Rändern jedoch atypische Banden. Diese zusätzlichen Signale korrelieren räumlich mit den durch Linienscans von Spurenelementen ermittelten Fe- und Ti-Profilen, was auf Gitterstörungen durch Fremdkationensubstitution zurückzuführen ist. Orientierungsmessungen bestätigen, dass die atypischen Banden vorwiegend durch defektbedingte Streuprozesse entstehen, die in E ∥ c weitgehend unterdrückt werden. Zusammenfassend zeigt die Arbeit, dass Diffusionsprozesse, Rutil-Ausscheidungen und Kationsubstitution gemeinsam die optischen und strukturellen Eigenschaften von synthetischem Sternkorund steuern. Die enge Übereinstimmung zwischen chemischen Gradienten und Raman-Signaturen unterstreicht die hohe Sensitivität der Vibrationsspektroskopie für diffusionsbedingte Defektstrukturen in Korund.

ABSTRACT (ENGLISH)

This thesis presents the results of a mineralogical characterisation of synthetic star corundum (yellow sapphire, blue sapphire and ruby) produced by Verneuil growth and subsequent Ti diffusion. All examined cabochons display a distinct six-rayed star generated by rutile needles in the diffusion rim. The blue sapphire is characterised by an intense diffusion zone with high Fe contents (8260 ± 290 ppm), while its core remains colourless. The ruby contains elevated Cr concentrations (3780 ± 150 ppm), consistent with its red colour, whereas the yellow sapphire shows colouration related to Mg-Fe trapped-hole centres. In all samples, unusually high Si concentrations (3730 ± 200 to 4090 ± 200 ppm) were detected, the origin of which remains unresolved. Raman spectroscopy reveals typical corundum spectra in the interiors but atypical spectra at the rims. These additional bands correlate spatially with Fe and Ti profiles obtained from trace-element linescans, suggesting that substitutional incorporation of cations of non-formula elements and related lattice distortions are responsible for the modified Raman response. Orientation-dependent measurements confirm that the atypical bands arise predominantly from defect-related scattering suppressed in E ∥ c configuration. In summary, the study demonstrates that diffusion processes, rutile precipitation, and cation substitution collectively govern the optical and structural properties of synthetic star corundum. The strong correlation between chemical gradients and Raman features highlights the sensitivity of vibrational spectroscopy to diffusion-related defect structures in corundum.

1. INTRODUCTION

Gemstones are known for their beautiful colour, and captivating cuts as well as for their intriguing optical effects. They arise due to the interaction of light with their internal structures. These effects include phenomena such as pleochroism, chatoyancy or ‘cat's eye effect’, and asterism, the ‘star effect’ (Hughes 2014; Bui et al. 2017; Belley 2023). In this study we analyse the phenomenon of asterism in synthetic corundum. It manifests as a star-shaped pattern of reflected light on the surface of the gem and is caused by the interaction of light with microscopic, needle-like inclusions or elongated cavities that align along the crystal’s axes (Wüthrich & Weibel 1981; Schmetzer et al. 2017). The star effect is not exclusive to corundum, for as other minerals such as diopside, garnet, and quartz can also exhibit this phenomenon (Freyer 1981; Doukhan et al. 1990; Guinel & Norton 2006).

Among the various minerals that exhibit optical effects, corundum holds a special place due to its unique combination of hardness, durability, and aesthetic appeal. Corundum, a crystalline form (trigonal space group $R\bar{3}c$) of aluminium oxide (Al_2O_3), is one of the hardest naturally occurring materials, ranking 9 on the Mohs scale. Naturally occurring corundum forms under high-pressure and high-temperature geological conditions and is commonly found in metamorphic and igneous rocks (Giuliani et al. 2014, p. 39). When pure, corundum is colourless; however, trace elements such as Fe, Ti, or Cr can impart various colours, leading to the formation of gemstones such as sapphires and rubies (Arkhangelskii et al. 1967; Wongrawang et al. 2016; Wu et al. 2022).

Due to its remarkable physical and optical properties, corundum has been highly valued throughout history, particularly in the field of gemmology. Both natural and synthetic sapphires and rubies can exhibit the optical effect of asterism, which makes them highly desirable in the jewellery market. A well-known example of natural star sapphire is the ‘Star of India’, one of the largest such gems in the world (Figure 1a). The American Museum of Natural History provided a photograph of this remarkable gemstone, which serves as an illustrative example of a natural star sapphire. Additionally, Figure 1b presents an image of synthetic star rubies of various sizes from Aue Gems Co., Ltd, displayed at a conference in Thailand. This visual comparison highlights the advancements in gemstone synthesis and the ability to engineer asterism under controlled conditions.

As synthetic star corundum becomes more sophisticated, the need to distinguish between natural and synthetic varieties has become increasingly important. The ability to differentiate them is crucial for gemmologists, traders, and collectors, as misidentification can affect market value and ethical considerations. Accurate characterisation relies on modern analytical techniques such as spectroscopy, microscopy, and EPMA analysis (electron probe microanalysis). These methods help determine the origin and properties of star corundum and

provide deeper insights into its composition, inclusions, and growth structures, enabling better classification and authentication.

This study aims to investigate the characteristics of synthetic star corundum, focusing on its physical, optical, and structural properties. By employing advanced analytical techniques, this research intends to identify distinct features that allow a clear differentiation from its natural counterpart. The findings of this study will contribute to the broader understanding of synthetic gemstone materials and their role in gemmological sciences and the jewellery industry.

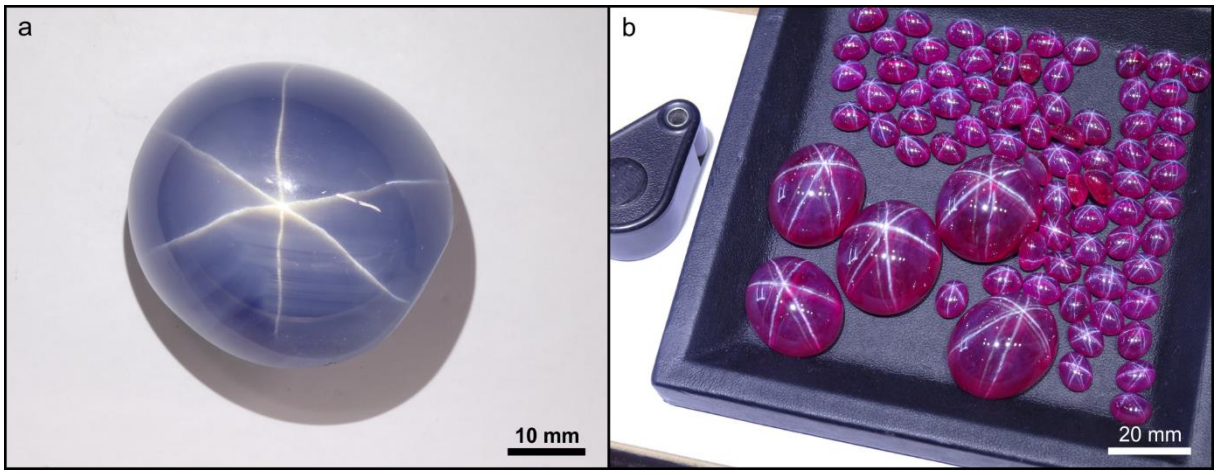

Figure 1: Both pictures show star corundum in a cabochon cut. (a) The 'Star of India', displayed at the American Museum of Natural History in New York City, is one of the world's largest gem-quality blue star sapphire at 563.35 ct (45 mm × 40 mm × 35 mm), featuring a flawless star on its surface and a distinct star on its back (photo taken by Andrea Mason). (b) High-quality star rubies, crafted from flame-fusion (Verneuil) synthetic cabochons up to 2.5 cm in size, showcased at the AUE Gems Co. Ltd booth at the 67th Bangkok Gems and Jewellery Fair in September 2022 (photo taken by Lutz Nasdala).

2. BACKGROUND INFORMATION: ASTERISM

2.1. Mineralogical and Crystallographic Basis of Asterism

The occurrence of asterism is dependent upon several crystallographic and mineralogical prerequisites. Primarily, the crystal system plays a critical role in the manifestation of this phenomenon. While asterism can arise in various crystallographic systems (including trigonal/hexagonal, orthorhombic, and cubic) certain crystal structures are particularly favourable.

Minerals belonging to the trigonal and hexagonal crystal systems are particularly conducive to displaying asterism due to their symmetrical structure and the orientation of inclusions along specific crystallographic axes (Schmetzer et al. 2017). Specifically, in these systems, the alignment of inclusions along the first and second hexagonal prism orders supports the formation of distinct star patterns. Natural and synthetic corundum develop their

needle-like inclusions within the basal plane, arranged in three distinct sets of oriented particles. These align parallel to the second hexagonal prism order faces $\{11\bar{2}0\}$, corresponding to the three <$10\bar{1}0$> crystallographic directions (Schmetzer et al. 2017). The inclusions responsible for asterism are typically minerals such as rutile (TiO_2), hematite (Fe_2O_3), ilmenite ($FeTiO_3$) or needle-like inclusions of other oxides (Moon & Phillips 1984; Hughes 1997; Viti & Ferrari 2006; Bui et al. 2017). In corundum, fine needles of rutile are often aligned in these three crystallographic directions intersecting at 120° angles, producing a characteristic six-rayed star. If there is a second group of acicular inclusions that are rotated by 30°, a twelve-rayed star is formed. These needles are then parallel to the first hexagonal prism order faces $\{10\bar{1}0\}$ (Hughes 1997).

Another example for a trigonal mineral with asterism is quartz. It shows six-rayed, twelve-rayed stars and multi-star networks (Schmetzter & Glas 2003). The star effect in quartz is in most cases the result of rutile inclusions. However, there are also star quartzes in which, for example, the needles are formed by sillimanite (Woensdregt et al. 1980). In special cases, three-rayed stars can also form in quartz. Gauthier et al. (2023) investigated the cause of the three-rayed 'Mercedes star' quartz and found that not only rutile needles are responsible for the optical effect, but that the combination of rutile needles and Brazi-law twins must be present.

There are also star minerals in orthorhombic systems. For example chrysoberyl — including its colour-changing variety alexandrite — crystallises in the orthorhombic system and can display either four- or six-rayed stars (Schmetzer et al. 2016). The difference arises from how the internal needles are aligned. A four-rayed star indicates two needle sets: one running parallel to the *a* axis [100], the other at 90° within the *bc* plane (Schmetzter 2010). When six rays appear, three needle sets lie in the plane perpendicular to the *a* axis (the (100) plane), producing the characteristic hexagonal star (Schmetzer & Hodgkinson 2011).

Even the cubic system supports asterism: in star garnet (typically almandine-pyrope) a four-rayed star forms when two perpendicular rutile-needle sets along <111> are visible, while the appearance of a third set along <011> adds a band of light and produces six rays (Schmetzer et al. 2002; Guinel & Norton 2006). This example reinforces the central point that the geometry of a star is governed by the orientation and number of inclusion families, not solely by the symmetry of the host lattice itself.

2.2. Historical Development of Synthetic Star Corundum

Although a variety of growth techniques exists – Czochralski pulling, flux and hydrothermal processes – to create synthetic corundum, to produce asteriated corundum the Verneuil flame-fusion method has proved sufficiently fast and economical for large-scale material (Hughes

1997; Bidney et al. 2010). Early commercial success was achieved by the Linde Air Products Company in the United States and, shortly afterwards, by Wiede's Carbidwerk in Germany (Breebaart 1957; Schmetzer et al. 2015).

During the 1940s and 1950s a portfolio of Linde patents set out the industrial blueprint for star corundum: Verneuil-grown boules were seeded with 0.1-0.3 wt% TiO_2, after which rutile was exsolved to produce the three intersecting light bands of a six-rayed star (Burdick & Glenn 1949). Linde's first-generation boules suffered from asterism confined to the outer "skin", leaving interior cabochons star-less and blue stones streaked with colourless sectors; the company therefore introduced cyclic adjustments to the oxy-hydrogen flame to disperse Ti more uniformly, an approach secured by a further patent (Burdick & Jones 1954; Eversole & Burdick 1954).

The 1954 patent of Eversole and Burdick outlined four practical demonstrations of post-growth TiO_2 diffusion to create or refine a star in corundum: (1) A colourless Verneuil sapphire boule was exposed to molten TiO_2 at ~1900 °C for six hours, then annealed 72 h at 1300 °C; a strong star developed on the treated surface. (2) Colourless sapphire and ruby cabochons were sprayed with slurries containing 100 wt%, 38 wt% or 10 wt% TiO_2, then heated for up to 24 h between 1800 °C and 1875 °C, followed by an annealing process of 72-96 h at 1300 °C. All stones became asteriated; the most uniform stars formed with a 38 wt% TiO_2 coating held 24 h at ~1800 °C. (3) A poorly starred synthetic blue sapphire cabochon was buried in granular TiO_2 and fired 12 h at 1950 °C, then re-annealed at 1300 °C. The treatment yielded a symmetrical, sharply defined star. (4) Cabochons of natural and synthetic sapphires in several colours were embedded in a 35 wt% TiO_2 : 65 wt% Al_2O_3 powder, heated 24-30 h at 1800 °C and annealed at 1300 °C. Each developed a well-defined six-rayed star within a thin, uniformly rutile-rich surface layer while the cores remained clear (Eversole & Burdick 1954).

Because those protections blocked direct imitation, Wiede's Carbidwerk developed an independent route. German patents DE 1 002 300 and DE 1 007 753 raised the TiO_2 content of the Verneuil feed to 0.52 wt%, lowered the powder-feed rate by at least half, and progressively shifted the O_2:H_2 ratio from 40:100 to 49:100. The outcome was an almost spherical, low-stress crystal in which rutile, precipitated during a 1100-1500 °C annealing process, was evenly distributed (Ancot & Eppler 1957a; b; Eppler 1958).

In 1972 Keig, Smith and Watts patented a pulled-boule technique (US 3 655 415) intended to grow synthetic star corundum with a uniformly dispersed Ti content, thereby avoiding the conspicuous banding typical of Verneuil stones (Keig et al. 1972) Technical success, however, was offset by prohibitive production costs, so the method never gained industrial traction and is remembered today mainly for its historical interest even though it produces larger crystals.

Carr and Nisevich (Carr & Nisevich 1975, 1976, 1977) further developed the diffusion technique originally introduced by Eversole and Burdick (1954) to modify the colour characteristics of natural and synthetic corundum. Their patents describe methods capable of enhancing or correcting uneven or unwanted colour distributions in both asteriated and non-asteriated ruby and sapphire crystals. Depending on the desired colour result, corundum is treated by diffusing one or more transition-metal oxides, such as those of Ti, Va, Cr, Fe, or Ni. To create or intensify asterism along with improving colour, an additional low-temperature annealing step is essential, allowing oriented precipitates containing Ti to form within the crystal structure.

Modern production of synthetic star corundum still heavily relies on Verneuil growth combined with diffusion treatments. The synthetic samples analysed in this study were similarly produced through Verneuil synthesis followed by Ti diffusion, making them representative of commercially available synthetic star corundum and thus suitable for a detailed gemmological and structural characterisation.

3. MATERIALS AND METHODS

The samples investigated in this study are synthetic star corundum specimens (sapphire and ruby) manufactured by Aue Gems Co., Ltd, Thailand. These specimens include three complete blue sapphire cabochons and two partial cabochons, one complete ruby cabochon, and one complete and two partial cabochons of yellow sapphire (Figure 2). To examine different crystallographic orientations, two samples from each colour variant (blue sapphire, yellow sapphire, and ruby) were precisely oriented and subsequently sliced parallel and perpendicular to the crystallographic c-axis. Sample orientation was conducted using an ENRAF-Nonius Kappa CCD X-ray diffractometer, applying a voltage of 50 kV, a current of 30 mA, and collecting ten frames for each measurement.

Figure 2: The image features three intact star corundum at the top: a yellow sapphire on the left, a blue sapphire in the centre, and a ruby on the right. In the lower-left corner, there is a half-cabochon of a yellow star sapphire, while the lower-right corner displays a disc of ruby cut parallel to the c-axis. In the centre, a disc of a blue sapphire is shown cut perpendicular to the c-axis, with the notable characteristic that the inner part of the sample is colourless, with only a very thin blue rim visible.

After orientation, slices of approximately 1 mm thickness were prepared using a Well diamond-wire saw. These slices were subsequently polished on both sides to achieve parallel planar surfaces using diamond powder (1 µm). The polished sections were neither fixed nor embedded but remained as independent, freely handled specimens. For post-Raman investigations, the polished slices were coated with a thin carbon film to enable electron-based imaging and quantitative microanalytical techniques. The carbon coating was deliberately applied only after Raman spectroscopy to avoid potential beam-induced alterations that may arise during electron beam exposure.

Gemmological properties were determined by measuring the refractive index using a KRÜSS refractometer from the BM series, coupled with a refractive index fluid with an nD of 1.78/1.79. Specific gravity was evaluated through repeated measurements on an analytical balance, initially weighing samples in air, followed by immersion in distilled water containing detergent to minimise surface tension effects, with each measurement performed five times to ensure reliability.

Microscopic examination of inclusions within the samples was conducted using a Keyence VHX 7000 digital microscope. Images were captured in reflected-light mode against a white backdrop, clearly highlighting needle-like inclusion patterns.

Raman spectroscopic measurements utilised a Horiba Scientific LabRAM HR Evolution spectrometer equipped with lasers emitting at wavelengths of 473 nm (blue) and 532 nm (green). Spectra were collected using a 100× objective (NA 0.90), combined with diffraction gratings of 1800 grooves/mm for Raman spectroscopy and 600 grooves/mm for photoluminescence (PL) analyses. These analyses were executed on polished slices without any additional preparatory procedures.

EPMA was performed on a CAMECA SXFive-FE instrument, operating at an acceleration voltage of 15 keV, probe currents of 150 nA and 180 nA, and utilizing a focused electron beam with a 1 µm diameter. The analyses focused on Al, Ti, and Fe, with quantitative linescans conducted radially inward from the sample edges, covering approximately 300 µm into the interior. A step size of 5 µm was applied for the first 100 µm from the rim, where the corundum-atypical structures are most pronounced, and 10 µm thereafter. All measurements were restricted to the respective Kα emission lines. Elemental calibration was performed using augite as a reference material. For each element, the peak was measured for 60 s, and the background was collected on both sides of the peak for 30 s. Raw X-ray intensities were measured relative to standard reference materials to obtain k-ratios, which were subsequently corrected using the PAP matrix correction algorithm to derive elemental weight concentrations (Pouchou & Pichoir 1991).

Trace element concentrations were further analysed using laser ablation-inductively coupled plasma-mass spectrometry (LA-ICP-MS). This analysis was carried out by coupling

an Agilent 7900 quadrupole ICP-MS with an ESI NWR193 laser ablation unit. The 193 nm laser operated at a repetition rate of 7 Hz with an energy density of approximately 4.0 J/cm² at the sample surface. Ablation was performed in line mode, with a spot size of 50 µm diameter, a total ablation length of 600 µm, and a scan speed of 10 µm/s. A dwell time of 25 ms per element was applied, except for Al, for which a shorter dwell time of 4 ms was used. Each ablation cycle consisted of an initial gas blank acquisition period of 25 s followed by 50 s of active sample ablation. The ablated material was carried to the ICP-MS system using helium gas at a flow rate of 0.8 L/min. Calibration of elemental concentrations was achieved using external reference standards NIST SRM610 and SRM612 (Jochum et al. 2011), while Al served as the internal standard element. Quality control was monitored by repeatedly measuring the USGS reference glass BCR-2G (Jochum et al. 2016), which yielded reproducibility within 5-10 % relative error. Data processing and reduction were conducted using the GLITTER 4.0 software (Griffin et al. 2008). Further methodological details are provided in Kruzslicz et al. (2020).

4. RESULTS AND DISCUSSION

4.1. General Properties

All examined cabochons are highly transparent and show a well-defined six-rayed star. The yellow sapphire and the ruby are uniformly coloured, whereas the blue sapphire possesses an intense diffusion rim while its core remains colourless (Figure 2). Beyond the oriented rutile needles that generate the asterism, no other inclusions were detected.

Hydrostatic weighing gave mean mass density of 3.997 ± 0.001 g/cm^{-3} for the ruby, 3.998 ± 0.003 g/cm^{-3} for the yellow sapphire and 3.997 ± 0.002 g/cm^{-3} for the blue sapphire. These values fall within the reference interval for corundum (mass density ≈ 3.98-4.06 g/cm^{-3}; Hughes 1997). Refractive indices measured 1.760-1.770, and are with that in full agreement with published data (Saito & Katsurada 2022).

All three varieties display distinct dichroism when observed in cross-polarised light. The largest cabochons weigh 5.5380 ct (ruby), 6.1985 ct (yellow sapphire) and 7.4495 ct (blue sapphire).

4.2. Chemical Composition

LA-ICP-MS analyses were used to investigate the chemical composition of the star corundum (Table 1). Aluminium totals cluster at 5.29 × 10^5 ppm in all three samples, confirming stoichiometric corundum. The Fe content (8260 ± 290 ppm) measured in near-surface areas of the blue sapphire is the highest of the three samples. It is far above the ≤ ≈ 1070 ppm

reported for melt-grown synthetics (Sun et al. 2017). Such a level indicates either an Fe-rich Verneuil feed or post-growth Fe diffusion, whereby a diffusion treatment is more likely due to the blue edge and the colourless centre. During manufacture most Ti precipitated as rutile needles that generate the star; the unbound remainder (~1386 ppm) can pair with Fe^{2+}, so Fe^{2+}–Ti^{4+} intervalence charge transfer (IVCT) would be the most plausible origin of the stone's blue colour. The role of the Si (3730 ± 200 ppm), Mg (19.45 ± 1.05 ppm) and Ni (7.95 ± 0.45 ppm) values for the Fe^{2+}–Ti^{4+} IVCT are explained in the work by Dubinsky et al. (2020).

Among the colour-forming transition metals for ruby, Cr is the principal dopant, reaching 3780 ± 150 ppm. This elevated Cr level is fully consistent with the intense red body colour and lies between the concentrations found in other synthetic rubies produced with the flame fusion method (≈1260-8750 ppm, calculated from the 0.184-2.41 t % Cr_2O_3 interval reported by Muhlmeister et al. 1998). The Fe content (190 ± 9 ppm) could be the reason why the ruby has a slightly pinkish hue (Dubinsky et al. 2020). Ruby contains a comparable amount of unbound Ti (1339 ± 55 ppm) to blue sapphire, but in the case of ruby it does not have another use.

The yellow star sapphire contains Mg = 153 ± 8 ppm, Fe = 748 ± 30 ppm, Ti = 625 ± 29 ppm, and Cr = 112.6 ± 5.3 ppm. Dubinsky et al. (2020) showed that even modest concentrations of (Fe^{3+}–h•) trapped-hole centres, stabilised by Mg^{2+} substitution, are sufficient to generate an intense yellow chroma in corundum. The simultaneous presence of Mg and Fe at the measured levels therefore accounts for the vivid body-colour observed here, while the comparatively low Cr content confirms that Cr does not contribute significantly to the hue.

To the best of my knowledge, there is currently no exact explanation in the literature for the very high silicon content. Kawaminami et al. (2013) attribute the presence of Si to the use of contaminated aluminium oxide powder in the production of ruby. However, the value in this sample seems somewhat too high for this explanation to be valid. They also state that it has no effect on the colour of the corundum. In contrast, Emmet et al. (2017) discuss the accuracy of Si content measurements using LA-ICP-MS, as AlH (with an atomic mass of 27.98936 amu) can be formed during ablation. This has a similar mass to Si (27.97693 amu) and is recognised as such by the detector. Together, these two sources could account for up to a few hundred ppm of Si, but not the much larger amounts of 3730 ± 200 ppm to 4090 ± 200 ppm observed here. The residual trace elements are either impurities inherent to the starting powder or contaminants that have infiltrated the material during the manufacturing process.

Optical absorption spectra of the three samples measured in two crystallographic orientations are shown in Figure A in Appendix A. However, these measurements did not yield sufficiently conclusive results to further support the colour interpretations discussed here.

Table 1: Trace-element concentrations (LA-ICP-MS results) of blue, yellow and red star-corundum samples.

Element	Isotope measured	Concentration [ppm]		
		Blue Sapphire	Yellow Sapphire	Ruby
Li	7	(bdl)	8.37 ± 0.44	1.01 ± 0.29
Be	9	(bdl)	0.99 ± 0.30	0.82 ± 0.26
B	11	5.96 ± 1.84	6.05 ± 1.48	13.0 ± 1.7
Mg	24	19.45 ± 1.05	153 ± 8	107.1 ± 4.8
Al	27	529000 ± 17000	529000 ± 17000	529000 ± 17000
Si	29	3730 ± 200	4090 ± 220	3810 ± 200
P	31	(bdl)	82.7 ± 16.8	110.8 ± 19.2
Sc	45	(bdl)	(bdl)	(bdl)
Ti	49	1386 ± 53	625 ± 29	1339 ± 55
V	51	0.36 ± 0.08	0.82 ± 0.09	0.50 ± 0.09
Cr	53	3.96 ± 1.04	112.6 ± 5.3	3780 ± 150
Mn	55	3.97 ± 0.52	7.00 ± 0.52	3.11 ± 0.48
Fe	56	8260 ± 290	748 ± 30	189.6 ± 8.8
Co	59	1.78 ± 0.11	1.06 ± 0.08	6.81 ± 0.29
Ni	60	7.95 ± 0.45	29.8 ± 1.3	19.2 ± 0.9
Cu	63	3.20 ± 0.20	39.9 ± 1.5	54.7 ± 1.9
Zn	66	5.83 ± 0.59	64.7 ± 2.9	57.0 ± 2.4
Ga	71	42.3 ± 1.5	37.0 ± 1.4	45.5 ± 1.6
Sr	88	0.06 ± 0.2	4.63 ± 0.20	1.39 ± 0.07
Y	89	(bdl)	0.91 ± 0.05	0.30 ± 0.02
Nb	93	0.07 ± 0.01	2.31 ± 0.10	0.16 ± 0.02
Zr	94	0.66 ± 0.10	1.78 ± 0.12	0.70 ± 0.09
Ba	137	(bdl)	1.39 ± 0.16	5.95 ± 0.35
Hf	178	(bdl)	(bdl)	0.70 ± 0.05
Ta	181	(bdl)	0.13 ± 0.01	0.59 ± 0.03
Pb	208	2.82 ± 0.17	6.37 ± 0.30	6.69 ± 0.30
Th	232	(bdl)	2.85 ± 0.12	0.15 ± 0.03
U	238	(bdl)	0.71 ± 0.05	0.08 ± 0.02

bdl: below the respective detection limit
All errors are quoted at the 1σ level.

4.3. Raman versus Photoluminescence

For each of the three samples, two spectra were recorded at two distinct points (Figure 3). At every measurement point, one spectrum was acquired using a 532 nm laser, and another using a 473 nm laser.

The blue sapphire exhibits an atypical spectrum at its edge (Figure 3a). Both spectra taken with the two different lasers demonstrate remarkably similar bands, allowing the conclusion that these represent genuine Raman bands rather than photoluminescence

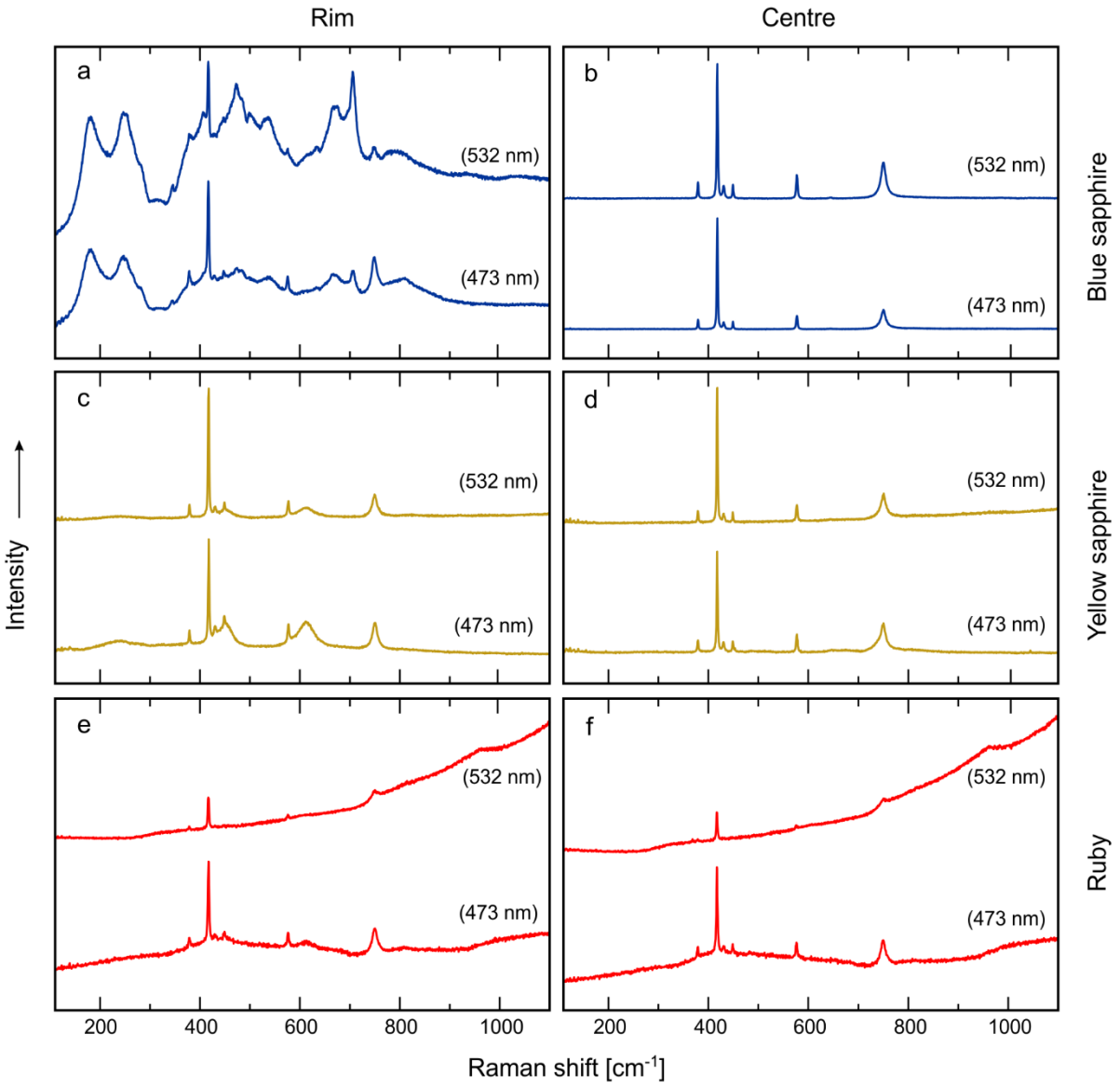

Figure 3: (a, b) Blue sapphire; (c, d) yellow sapphire; (e, f) ruby. For each location two spectra are plotted: 532 nm excitation (upper trace) and 473 nm excitation (lower trace). Because the band pattern is identical for both lasers, all features are verified as Raman bands, not laser-induced photoluminescence. The ruby spectra show a rising baseline caused by uniform Cr^{3+} fluorescence. Only the blue sapphire displays an atypical rim spectrum that vanishes toward the colourless core. The yellow sapphire shows merely very weak rutile bands, probably from a single needle intersecting the laser spot.

artifacts. Figure 3b reveals a marked contrast compared to Figure 3a, clearly displaying the typical corundum spectrum already documented extensively in previous publications.

Likewise, the corundum bands are distinctly visible in the yellow sapphire spectra shown in Figures 3c and 3d. Additionally, faint rutile bands can be identified in both spectra of Figure 3c. This finding is not surprising, as needle-like inclusions observed at the edge of the star corundum are expectedly composed of rutile, causing contamination of the corundum spectra.

The spectra of the ruby also clearly exhibit the characteristic corundum bands. However, an upward slope is noticeable, attributable to strong luminescence, which significantly elevates the spectral baseline.

4.4. Comparison of Raman spectra

The Raman spectra are plotted in Figure 4 to compare the atypical spectra of the blue sapphire with the spectra of a typical corundum and the rutile needles. The recorded spectrum of the needles corresponds well with literature data and with the rutile reference material (Frank et al. 2012). Within the blue sapphire, the rutile does not only exhibit the well-known rutile Raman bands (~140, ~235, ~440, and ~610 cm^{-1}) but also additional bands clearly attributable to corundum, an expected effect because the needles are extremely narrow and the laser spot unavoidably samples both the inclusion and the host.

Initial spot analyses taken near the crystal edge (~10 µm from the surface) revealed an atypical Raman spectrum for corundum: the strongest corundum bands are present, but numerous additional bands appear that are absent from spectra collected deeper in the crystal (~900 µm). Comparable, atypical corundum spectra (i.e., spectra that either display extra bands or show departures from the ideal pattern) have been published in both natural and synthetic contexts, yet were typically presented without in-depth discussion of their origin (Jbara et al. 2017; Myšľan et al. 2024). Yu et al. (2019) report a band near ~245 cm^{-1}, which they assign to an E_g vibration associated with Fe^{3+} displacement, however without providing any explanation for this interpretation. This assignment may be related to observations by Yu et al. (2015), who documented a band at ~245 cm^{-1} in the Raman spectrum of Fe_2O_3. However, the absence of other characteristic hematite bands was not addressed in their discussion. A more explicit interpretation is provided by Fu et al. (2020) for recrystallised corundum, which exhibits a similarly atypical corundum spectrum. The authors noted that some characteristic Raman bands may be weakened, distorted, or shifted and relate this behaviour to lattice distortions caused by the uneven incorporation of impurity ions during processing.

A second study supports this view and adds detail. Mazza et al. (2007) systematically doped ceria (CeO_2) with increasing amounts of Gd and observed progressively larger

departures from the Raman spectrum of the undoped material. Because grain-size effects in their setup produced only minor broadening, they concluded that substitutional disorder has a much stronger impact on the Raman band shape than grain-size-induced non-stoichiometry. This pattern aligns with our sapphire results. At the blue rim, where Fe and Ti have diffused in, the atypical corundum spectrum is observed, whereas the colourless interior reverts to the canonical response. By analogy, substitution of cations of non-formula elements in the rim zone could contribute to the non-ideal spectrum observed in the blue sapphire, although other defect-related mechanisms may also be involved.

In the violet-black fluorites (antozonite) described by Čermáková et al. (2015), the Raman spectra are likewise strongly altered compared with those of pure, white synthetic fluorite without impurities. The colouration is attributed to natural irradiation, which produced structural dislocations in the crystal lattice. The authors consider it likely that the distinctive Raman bands of antozonite are related to radiation-induced point defect complexes. The

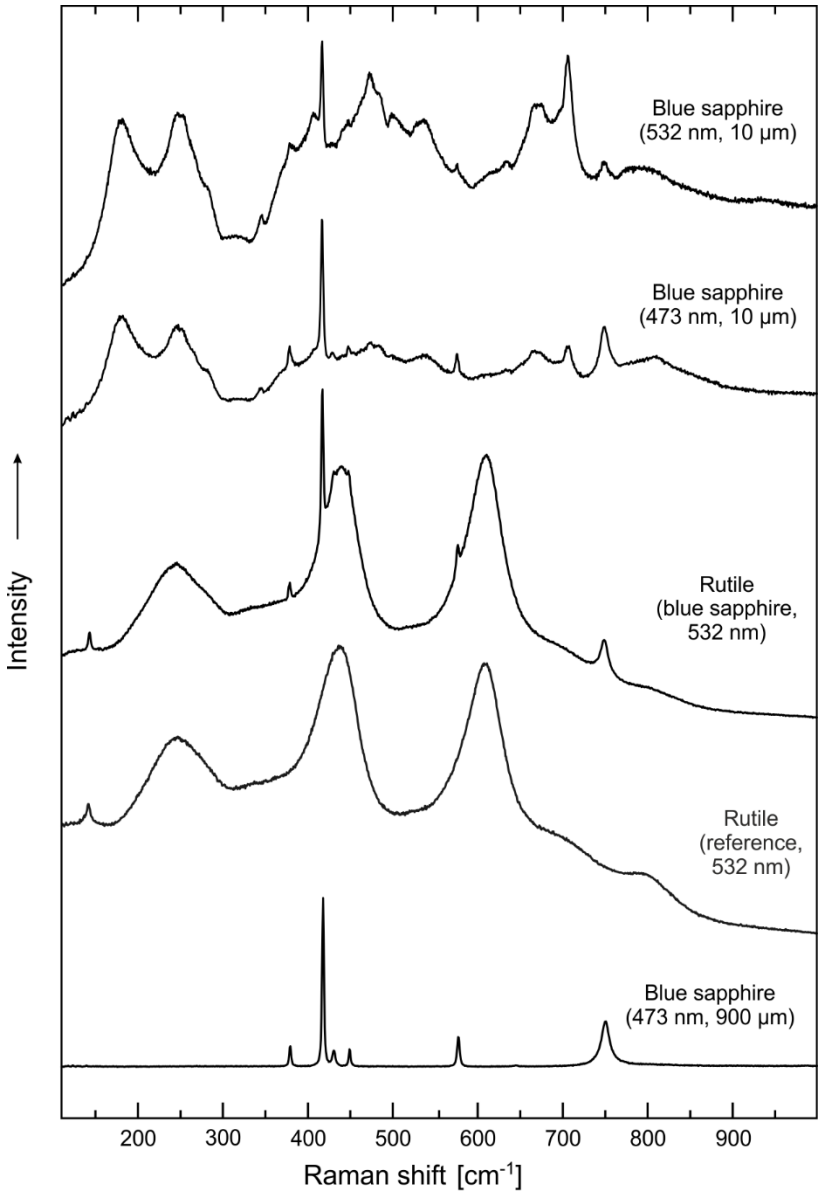

Figure 4: The top two spectra were both collected from the blue sapphire 10 µm inside the rim, but with different laser wavelengths (532 nm and 473 nm). The next two spectra display rutile bands; the upper of these was recorded in the blue sapphire and also contains bands of the corundum host lattice. This matches the bottom spectrum, which was obtained with a blue (473 nm) laser in the colourless region, 900 µm from the rim.

synthetic blue sapphire examined here was certainly not irradiated, so the defects must have a different origin; nevertheless, this example illustrates that such spectral changes can arise from point defects.

Another potential cause is the presence of nanophases, such as colloidal particles. Wesełucha-Birczyńska et al. (2012) examined blue halite which is normally Raman-inactive, but in this case showed a distinct band near ~200 cm^{-1} that they attributed to colloidal particles. Although the chemical composition differs from sapphire, this example illustrates how nanoscale inclusions can generate additional low-wavenumber Raman features.

Finally, diffusion-related mechanisms may also contribute. Sastry et al. (2009) demonstrated that Be-diffusion in corundum can profoundly alter both Raman and infrared spectra by disturbing the long-range order of the lattice. In Be-treated sapphires, characteristic vibrational bands were either weakened or disappeared entirely, and broad amorphous-like features developed instead. The authors attributed this to substitutional and charge disorder, the dissolution of inclusions, and associated glass formation, ultimately leading to lattice instability and partial loss of crystallinity. By analogy, similar diffusion-driven disorder mechanisms (whether induced by Be or other heterovalent cations) could also be responsible for the atypical Raman response observed in the blue sapphire rim.

4.5. Orientation dependency

Six Raman spectra were collected from the blue sapphire: three in the E ⊥ c configuration (Figure 5, top) and three in E ∥ c (Figure 5, bottom). For each orientation, two spectra were acquired near the sample's rim with 473 nm and 532 nm excitation, together with a 532 nm reference spectrum from the colourless centre.

In the centre, only the well-known, sharp corundum modes are observed; identical band positions with 473 nm and 532 nm excitation confirm their Raman origin. At the rim, additional, broader and partly complex bands appear. These are strongly orientation dependent: they are pronounced in E ⊥ c but strongly suppressed in E ∥ c, while the canonical corundum modes are particularly intense in E ∥ c.

Corundum exhibits Raman-active A_{1g} and E_g modes. The polarisation dependence follows from the Raman tensors: in the c-parallel geometry (E ∥ c), A_{1g} contributions dominate, and many E_g terms are attenuated; in E ⊥ c, E_g modes are preferentially excited and detected. This naturally explains the orientation contrast at the rim, the atypical bands couple predominantly via E_g-like (in-plane) polarizability changes and therefore largely vanish in E ∥ c, whereas the A_{1g}-dominated corundum modes brighten in E ∥ c (Munisso et al. 2009; Pezzotti & Zhu 2015).

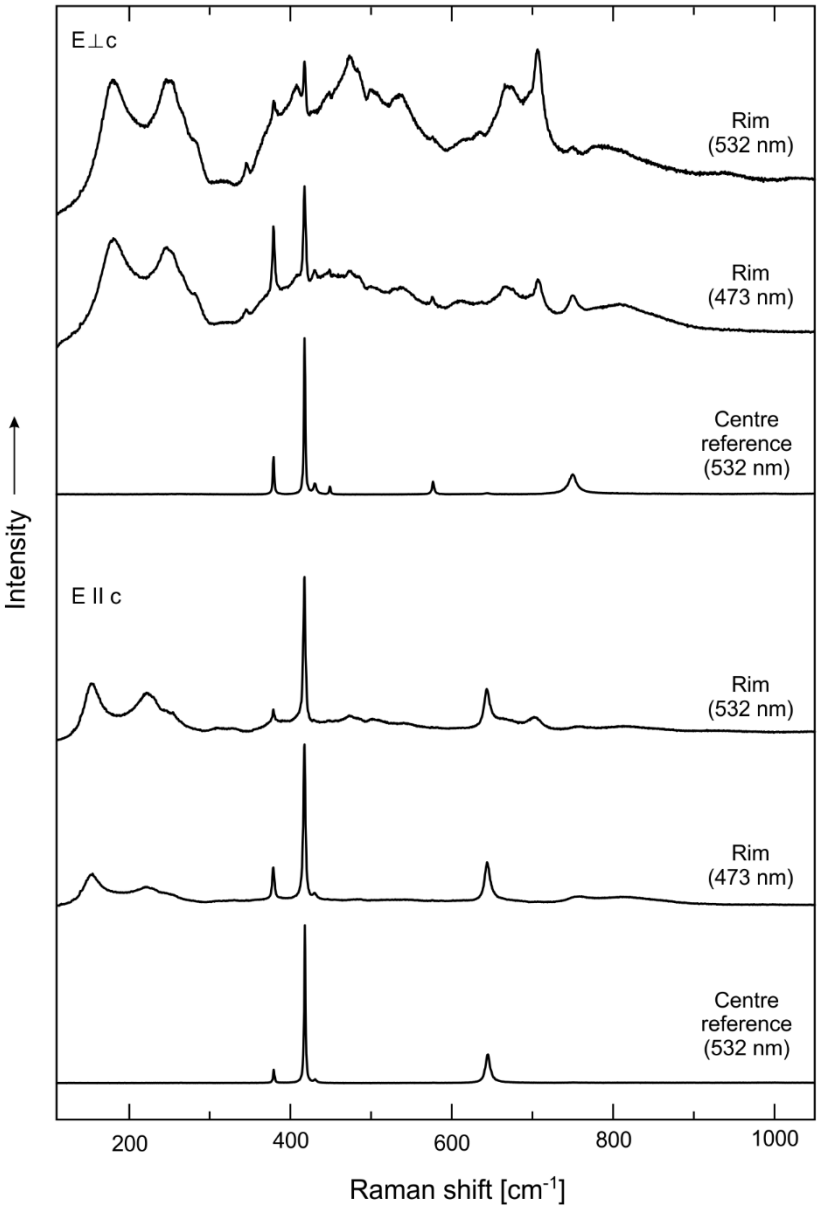

Figure 5: Raman spectra of the blue sapphire collected in two polarisation geometries relative to the optical c-axis: E ⊥ c (top three traces) and E ∥ c (bottom three traces). For each geometry, two spectra were acquired near the sample's rim (473 and 532 nm excitation) exhibit an atypical, broadband pattern, whereas the colourless centre (reference, 532 nm) shows only the canonical corundum modes. The spectra with the atypical bands are strongly orientation-dependent: they are pronounced for E ⊥ c but largely suppressed for E ∥ c, while the corundum modes are correspondingly intense in E ∥ c. Identical band positions for both laser lines confirm that all sharp features are genuine Raman modes rather than PL.

The rim region typically exhibits elevated defect densities, micro-/nanoscopic strain, doping/compositional gradients, or nanoscale nuclei of other phases. If, in the E ∥ c configuration, the "atypical" bands weaken while the corundum bands become more distinct, this points to the atypical signals originating from symmetry breaking/disorder. Such effects, likely driven by the aforementioned defect density, are largely suppressed in this orientation because the selection rules filter out much of the "forbidden" scattering.

4.6. Microstructure and Diffusion Profiles

In the following section, the characteristic microstructures of the diffusion rim and the associated chemical profiles of Fe and Ti are examined. The dark-field electron microscopic image of the blue sapphire (Figure 6a) displays a pronounced, bright-blue rim characterised

by densely developed needle-shaped rutile crystals. These needles progressively decrease toward the sample interior and eventually vanish. The bright-field image (Figure 6b) illustrates the gradual diffusion zone: the blue colouration is most intense in the area of needle occurrence and systematically decreases with increasing distance from the rim.

Quantitative EPMA line analyses (Figure 6c) provide concentration profiles of Fe (black) and Ti (blue) across a distance of 0 - ≈ 330 µm. Both elements exhibit a steep decline within the first ≈ 50 µm from the rim and approach the background concentration of the non-diffused material at approximately 300 µm. The asymmetry of the decline and the differing slopes of

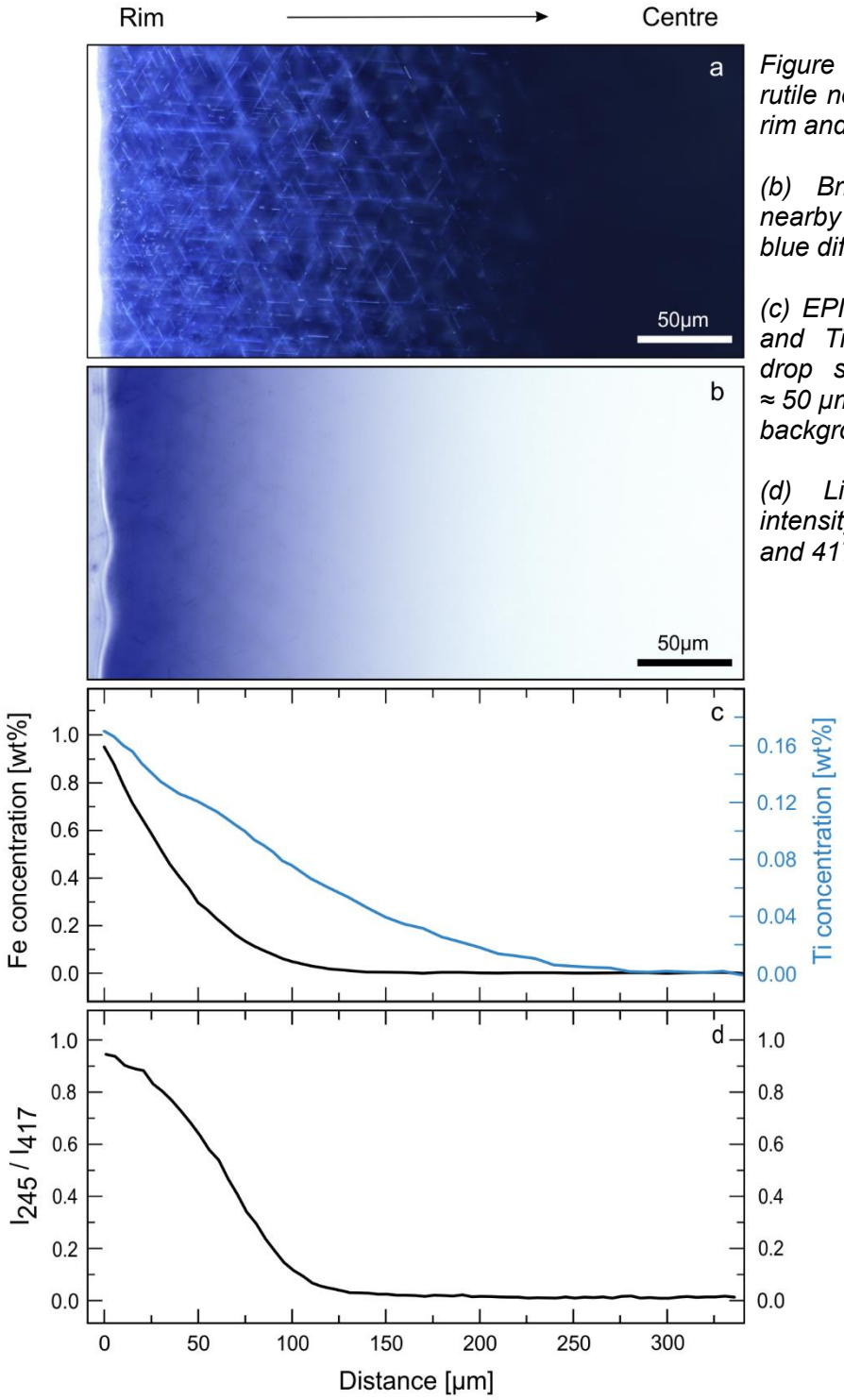

Figure 6: (a) Dark-field image: rutile needles are dense at the rim and fade inwards.

(b) Bright-field image of a nearby region, illustrating the blue diffusion rim.

(c) EPMA linescan: Fe (black) and Ti (blue) concentrations drop steeply within the first ≈ 50 µm and approach background by ≈ 300 µm.

(d) Linescan showing the intensity ratio of the 245 cm^{-1} and 417 cm^{-1} Raman bands.

the two profiles indicate slightly different diffusion coefficients, with Ti diffusing marginally more slowly than Fe. Comparable features are observed in ruby (Figure B1 in Appendix B) and yellow sapphire (Figure B2). For these two samples, only Ti was chemically analysed, but the results are consistent with the presence of rutile needles.

In addition to the distribution of Fe and Ti, the occurrence of the unusual spectrum was investigated. A Raman linescan was performed, and the intensity ratio of the bands at 245 cm^{-1} (atypical spectrum) and 417 cm^{-1} (typical corundum band) was calculated and plotted (Figure 6d). This approach allows the spatial distribution of the unusual spectrum in blue sapphire to be assessed. The intensity ratio decreases from its maximum at the outer rim to nearly zero in the interior. The resulting curve closely parallels the concentration profiles of Fe and Ti, suggesting a relationship between elemental diffusion and the appearance of the unusual spectrum.

According to the model proposed by Mazza et al. (2007), structural distortions induced by cation substitutions are likely to modify the Raman spectrum. Figure 6 clearly demonstrates that in the zone affected by Fe and Ti diffusion, the Raman spectrum is significantly altered. This correspondence supports the interpretation that the unusual spectral features arise from lattice distortions associated with the incorporation of cations of non-formula elements. The parallel behaviour of elemental concentration profiles and spectral intensity ratios further suggests that the extent of diffusion directly governs the degree of structural perturbation. Consequently, the atypical Raman bands may serve as a sensitive indicator of diffusion-related defect structures in synthetic corundum.

5. CONCLUSIONS

This study has provided a detailed characterisation of synthetic star corundum through a combination of gemmological, spectroscopic, and microanalytical methods. While the results confirm key aspects already known from earlier, they also highlight several open questions and promising directions for further investigation.

A particularly relevant avenue concerns the quantification of diffusion mechanisms. The distinct profiles of Fe and Ti observed in this study suggest differences in diffusion behaviour, but the kinetics remain insufficiently constrained. Systematic high-temperature diffusion experiments would help determine reliable diffusion coefficients and clarify their role in colour development, defect formation, and rutile precipitation.

The atypical Raman spectra identified at the diffusion rims likewise merit deeper investigation. Their correlation with elemental profiles strongly suggests a link to substitutional disorder and lattice distortions, yet the precise structural mechanisms remain unresolved. Complementary techniques such as transmission electron microscopy, synchrotron-based

spectroscopy, or atom probe tomography could provide nanoscale insights and validate Raman spectroscopy as a diagnostic tool for defect structures in corundum.

Another unresolved aspect is the unusually high silicon content consistently detected in the samples. Future studies should evaluate whether this anomaly arises from contamination in starting materials, instrumental artefacts, or a yet unrecognised incorporation mechanism. Cross-comparisons between different analytical methods and systematic analyses of feed powders would be particularly valuable here.

Finally, while this work has focused exclusively on synthetic samples, comparative studies involving natural star corundum remain essential. Such investigations would provide a broader framework for interpreting diffusion profiles, defect structures, and inclusion patterns, thereby strengthening the ability to place synthetic material in context with natural analogues.

In sum, this study contributes to the ongoing research on synthetic star corundum by characterising its physical, chemical, and optical properties, and by pointing to critical open questions regarding diffusion, defect formation, and trace-element incorporation. Addressing these questions through targeted future research will not only refine our understanding of synthetic gemstone materials but also deepen the broader mineralogical knowledge of corundum as a host lattice for complex diffusion and defect processes.

6. REFERENCES

Ancot, E. & Eppler, W.F. 1957a. Verfahren zur Herstellung synthetischer, Asterismus aufweisender Korunde. DE Patent 1002300, issued 14 August 1957.

Ancot, E. & Eppler, W.F. 1957b. Verfahren zur Herstellung von synthetischen Sternkorunden. DE Patent 1007753, issued 24 October 1957.

Arkhangelskii, G.K., Morgenshtern, Z.L. & Neustruev, V.B. 1967. Colour Centres in Ruby Crystals. *physica status solidi (b)*, **22**(1), 289–295, https://doi.org/10.1002/pssb.19670220134.

Belley, P.M. 2023. Iolite from the Thor-Odin Dome, British Columbia, Canada: Geology, Chemical Composition, Inclusions, and Cause of Chatoyancy. *Gems & Gemology*, **59**(3), 340–355, https://doi.org/10.5741/gems.59.3.340.

Bidney, A.S., Dolgova, O.S., Baksheev, I.A. & Ekimenkova, I.A. 2010. New data for distinguishing between hydrothermal synthetic, flux synthetic and natural corundum. *The Journal of Gemmology*, **32**(1), 7–13, https://doi.org/10.15506/jog.2010.32.1-4.7.

Breebaart, A.J. 1957. Structure & Inclusions of synthetic star-stones. *The Journal of Gemmology*, **6**(2), 72–74, http://dx.doi.org/10.15506/JoG.1957.6.2.72.

Bui, T., Entremont, P. & Gauthier, J.-P. 2017. Large 12-Rayed Black Star Sapphire from Sri Lanka with Asterism Caused by Ilmenite Inclusions. *The Journal of Gemmology*, **35**(5), 430–435, https://doi.org/10.15506/JoG.2017.35.5.430.

Burdick, J.N. & Glenn, J.J.W. 1949. Synthetic star rubies and star sapphires, and process for producing same. US Patent 2,488,507, issued 15 November 1949.

Burdick, J.N. & Jones, R.A. 1954. Synthetic corundum crystals and process for making same. US Patent 2,690,062, issued 28 September 1954.

Carr, Ronald. & Nisevich, S.D. 1975. Altering the appearance of corundum crystals. US Patent 3,897,529, issued 29 July 1975.

Carr, R.R. & Nisevich, S.D. 1976. Altering the appearance of corundum crystals. US Patent 3,950,596, issued 13 April 1976.

Carr, R.R. & Nisevich, S.D. 1977. Altering the appearance of corundum crystals. US Patent 4,039,726, issued 2 August 1977.

Čermáková, Z., Bezdička, P., Němec, I., Hradilová, J., Šrein, V., Blažek, J. & Hradil, D. 2015. Naturally irradiated fluorite as a historic violet pigment: Raman spectroscopic and X-ray diffraction study. *Journal of Raman Spectroscopy*, **46**(2), 236–243, https://doi.org/10.1002/jrs.4627.

Doukhan, N., Ingrin, J., Doukhan, J.C. & Latrous, K. 1990. Coprecipitation of magnetite and amphibole in black star diopside: A TEM study. *American Mineralogist*, **75**(7–8), 840–846.

Dubinsky, E.V., Stone-Sundberg, J. & Emmett, J.L. 2020. A Quantitative Description of the Causes of Color in Corundum. *Gems & Gemology*, **56**(1), 2–28, https://doi.org/10.5741/gems.56.1.2.

Eppler, W.F. 1958. Notes on Asterism in corundum, rose quartz and almandine garnet and chatoyancy in beryl. *The Journal of Gemmology*, **6**(5), 195–212, https://doi.org/10.15506/jog.1958.6.5.195.

Eversole, W.G. & Burdick, J.N. 1954. Producing asteriated corundum crystalls. US Patent 2,690,630, issued 5 October 1954.

Frank, O., Zukalova, M., Laskova, B., Kürti, J., Koltai, J. & Kavan, L. 2012. Raman spectra of titanium dioxide (anatase, rutile) with identified oxygen isotopes (16, 17, 18). *Physical Chemistry Chemical Physics*, **14**(42), 14567–14572, https://doi.org/10.1039/c2cp42763j.

Freyer, C. 1981. Gem Trade Lab Notes: Star Quartz. *Gems & Gemology*, **17**(4), 230.

Fu, J., Lyu, F. & Shao, T. 2020. Gemmological Chraracteristic of 'Recrystallized' (Synthetic) Corundum in Market. *Journal of Gems & Gemology*, **22**(6), 9–19.

Gauthier, J.-P., Fritsch, E., Bui, T.N. & Fereire, J. 2023. Clues to Understanding the Enigma of the Unusual Asterism in 'Mercedes-Star' Quartz. *The Journal of Gemmology*, **38**(7), 678–695, https://doi.org/10.15506/jog.2023.38.7.678.

Giuliani, G., Ohnenstetter, D., Fallick, A.E., Groat, L. & Fagan, A. 2014. The geology and genesis of gem corundum deposits. *In: Groat, L. (ed) Geology of Gem Deposits*. , Québec, Canada, 29–112.

Griffin, W.L., Powell, W.J., Pearson, N.J. & O'Reilly, S.Y. 2008. APPENDIX A2: GLITTER: DATA REDUCTION SOFTWARE FOR LASER ABLATION ICP–MS. *In: Sylvester, P. (ed) Laser Ablation ICP-MS in the Earth Sciences: Current Practices and Outstanding Issues*. , Québec, Canada, 308–311.

Guinel, M.J.-F. & Norton, M.G. 2006. The origin of asterism in almandine-pyrope garnets from Idaho. *Journal of Materials Science*, **41**(3), 719–725, https://doi.org/10.1007/s10853-006-6500-4.

Hughes, R.W. 1997. *Ruby & sapphire.* RWH Publishing, Colorado, USA, 511 pp.

Hughes, R.W. 2014. Pleochroism in faceted gems: an introduction. *Gems & Gemology*, **50**(3), 216–226, https://doi.org/10.5741/gems.50.3.216.

Jbara, A.S., Othaman, Z., Ati, A.A. & Saeed, M.A. 2017. Characterization of g- Al2O3 nanopowders synthesized by Coprecipitation method. *Materials Chemistry and Physics*, **188**, 24–29, http://dx.doi.org/10.1016/j.matchemphys.2016.12.015.

Jochum, K.P. et al. 2011. Determination of Reference Values for NIST SRM 610–617 Glasses Following ISO Guidelines. *Geostandards and Geoanalytical Research*, **35**(4), 397–429, https://doi.org/10.1111/j.1751-908X.2011.00120.x.

Jochum, K.P. et al. 2016. Reference Values Following ISO Guidelines for Frequently Requested Rock Reference Materials. *Geostandards and Geoanalytical Research*, **40**(3), 333–350, https://doi.org/10.1111/j.1751-908X.2015.00392.x.

Keig, G.A., Smith, J.C. & Watts, J.M.J. 1972. Asteriated synthetic corundum gem stones and method and apparatus for their production. US Patent 3,655,415, issued 11 April 1972.

Kruzslicz, Á.B., Nasdala, L., Wildner, M., Škoda, R., Redhammer, G.J., Hauzenberger, C. & Wanthanachaisaeng, B. 2020. Black spinel - a gem material from Bo Phloi, Thailand. *The Journal of Gemmology*, **37**(1), https://doi.org/10.15506/jog.2020.37.1.

Moon, A.R. & Phillips, M.R. 1984. An electron microscopy study of exsolved phases in natural black Australian sapphire. *Micron and Microscopica Acta*, **15**(3), 143–146, https://doi.org/10.1016/0739-6260(84)90044-3.

Muhlmeister, S., Fritsch, E., Shigley, J.E., Devouard, B. & Laurs, B.M. 1998. Separating Natural and Synthetic Rubies on the Basis of Trace-Element Chemistry. *Gems & Gemology*, **34**(2), 80–101, https://doi.org/10.5741/gems.34.2.80.

Munisso, M.C., Zhu, W. & Pezzotti, G. 2009. Raman tensor analysis of sapphire single crystal and its application to define crystallographic orientation in polycrystalline alumina. *physica status solidi (b)*, **246**(8), 1893–1900, https://doi.org/10.1002/pssb.200945137.

Myšľan, P., Števko, M. & Vaculovič, T. 2024. Mineralogy and genesis of sapphire in corundum-bearing xenoliths from the Miocene andesites in the Záhradné, Hubošovce and Vechec quarries in the Slanské vrchy Mountains (Slovakia). *Geologica Carpathica*, **75**(2), 117–131, https://doi.org/10.31577/geolcarp.2024.06.

Pezzotti, G. & Zhu, W. 2015. Resolving stress tensor components in space from polarized Raman spectra: polycrystalline alumina. *Physical Chemistry Chemical Physics*, **17**(4), 2608–2627, https://doi.org/10.1039/C4CP04244A.

Pouchou, J.-L. & Pichoir, F. 1991. Quantitative Analysis of Homogeneous or Stratified Microvolumes Applying the Model “PAP”. *In: Heinrich, K.F.J. & Newbury, D.E. (ed) Electron Probe Quantitation*. , Boston, MA, 31–75.

Saito, M. & Katsurada, Y. 2022. Lab Note: Combination of phenomena in star and cat’s-eye color-change sapphire. *Gems & Gemology*, **58**(2), 222–223.

Sastry, M.D., Mane, S.N., Gaonkar, M.P., Bagla, H., Panjikar, J. & Ramachandran, K.T. 2009. Evidence of colour-modification induced charge and structural disorder in natural corundum: Spectroscopic studies of beryllium treated sapphires and rubies. *IOP Conf. Ser.: Mater Sci Eng*, **2**(1), 012007, https://doi.org/10.1088/1757-899X/2/1/012007.

Schmetzer, K., Bernhardt, H.-J. & Gilg, H.A. 2016. Characterization of Oriented Inclusions in Cat’s-eye, Star and Other Chrysoberyls. *The Journal of Gemmology*, **35**(1), 28–53, https://doi.org/10.15506/jog.2016.35.1.28.

Schmetzer, K., Bernhardt, H.-J. & Kiefert, L. 2002. Star garnets and star garnet cat’s-eyes from Ambatondrazaka, Madagascar. *The Journal of Gemmology*, **28**(1), 66, https://doi.org/10.15506/jog.2002.28.1.13.

Schmetzer, K., Gilg, H.A. & Bernhardt, H.-J. 2017. Synthetic star sapphires and rubies produced by Wiede’s Carbidwerk, Freyung, Germany. *Gems & Gemology*, **53**(3), 312–324, https://doi.org/10.5741/gems.53.3.312.

Schmetzer, K. & Hodgkinson, A. 2011. Synthetic star alexandrite. *Gems & Jewellery*, **20**(3), 9–11.

Schmetzer, K., Steinbach, M.P., Gilg, H.A. & Blake, A.R. 2015. Dual-Color Double Stars in Ruby, Sapphire, and Quartz: Cause and Historial Account. *Gems & Gemology*, **51**(2), 112–143, https://doi.org/10.5741/gems.51.2.112.

Schmetzter, K. 2010. *Russian Alexandrites.* Schweizerbart Science Publishers, Stuttgart, 141 pp.

Schmetzter, K. & Glas, M. 2003. Multi-star quartzes from Sri Lanka. *The Journal of Gemmology*, **28**(6), 321–332, https://doi.org/10.15506/jog.2003.28.6.321.

Sun, Z., Muyal, J. & Ahline, N. 2017. Lab Note: Multi-elemental diffused and melt-grown synthetic sappire. *Gems and Gemology*, **53**(1), 98–99.

Viti, C. & Ferrari, M. 2006. The nature of Ti-rich inclusions responsible for asterism in Verneuil-grown corundums. *European Journal of Mineralogy*, **18**(6), 823–834, https://doi.org/10.1127/0935-1221/2006/0018-0823.

Wesełucha-Birczyńska, A., Zelek, S. & Stadnicka, K. 2012. Blue halite colour centre aggregates studied by micro-Raman spectroscopy and X-ray diffraction. *Vibrational Spectroscopy*, **60**, 124–128, 10.1016/j.vibspec.2011.11.001.

Woensdregt, C.F., Weibel, M. & Wessicken, R. 1980. Star Quartz Asterism caused by Sillimanite. *Schweizerische mineralogische und petrologische Mitteilungen*, **60**(2–3), 129–132, https://doi.org/10.5169/seals-46662.

Wongrawang, P., Monarumit, N., Thammajak, N., Wathanakul, P. & Wongkokua, W. 2016. Oxidation states of Fe and Ti in blue sapphire. *Materials Research Express*, **3**(2), https://doi.org/10.1088/2053-1591/3/2/026201.

Wu, X., Han, X., Kang, Y., Feng, X. & Guo, S. 2022. Effect of Reduction Annealing on the Coloration Mechanism of Yellow Sapphire with High Iron Content. *Crystals*, **12**(9), https://doi.org/10.3390/cryst12091257.

Wüthrich, A. & Weibel, M. 1981. Optical theory of asterism. *Physics and Chemistry of Minerals*, **7**(1), 53–54, https://doi.org/10.1007/BF00308202.

Yu, J., He, X. & Lu, Z. 2019. Cause analysis of chatoyancy of sapphires from Shandong, China. *RSC Advances*, **9**(42), 24420–24427, https://doi.org/10.1039/c9ra03585k.

Yu, X., Niu, X. & Zhao, L. 2015. Characterization and Origin of Zonal Sapphire from Shandong Province, China. *JOM*, **67**(2), 391–397, https://doi.org/10.1007/s11837-014-1270-y.

7. LIST OF FIGURES

8. LIST OF TABLES

APPENDIX

Appendix A: Optical Absorption spectra

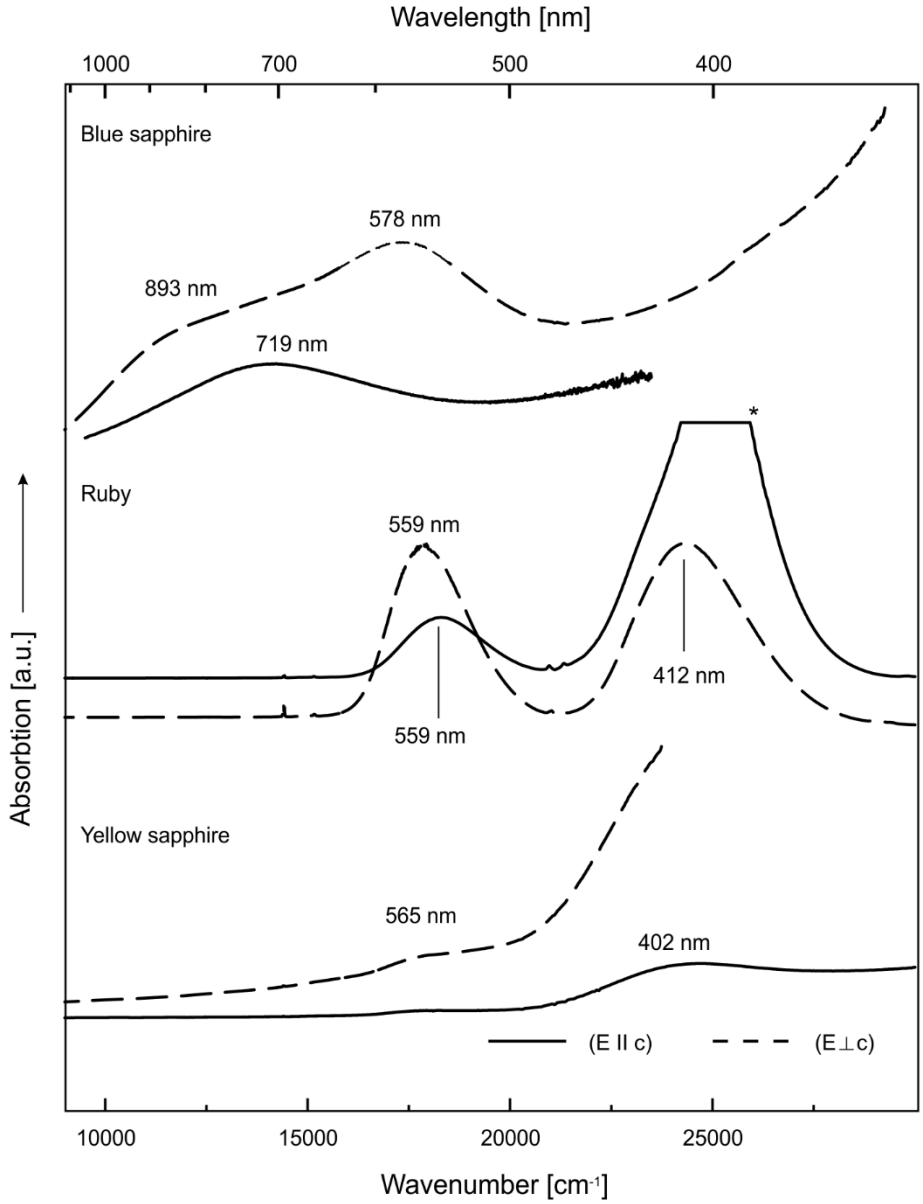

*Abb. A 1: Optical absorption spectra of synthetic star corundum varieties (blue sapphire, ruby, and yellow sapphire) measured in two crystallographic orientations (solid line: E ∥ c , dashed line: E ⊥ c). Characteristic absorption bands are indicated by their respective wavelengths. The region marked with * was truncated due to excessive noise.*

Appendix B: Microstructure and Diffusion Profiles

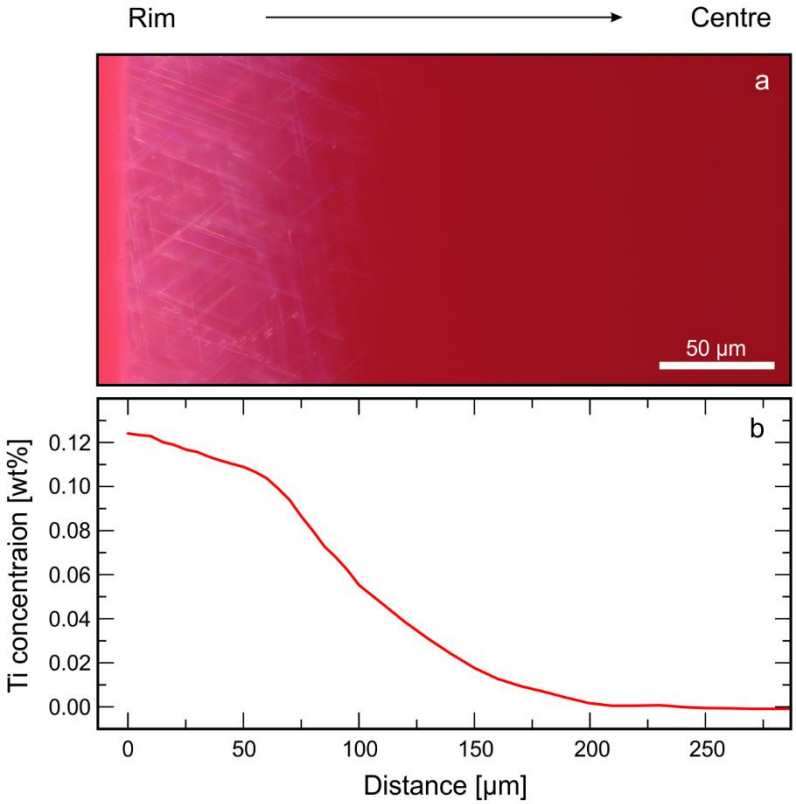

Abb. B 1: (a) Dark-field image (scale = 50 µm) with dense rutile needles in the red diffusion rim that diminish toward the crystal centre.

(b) EPMA linescan: Ti concentration declines from ~ 0.12 wt% at the rim to < 0.01 wt% beyond 250 µm.

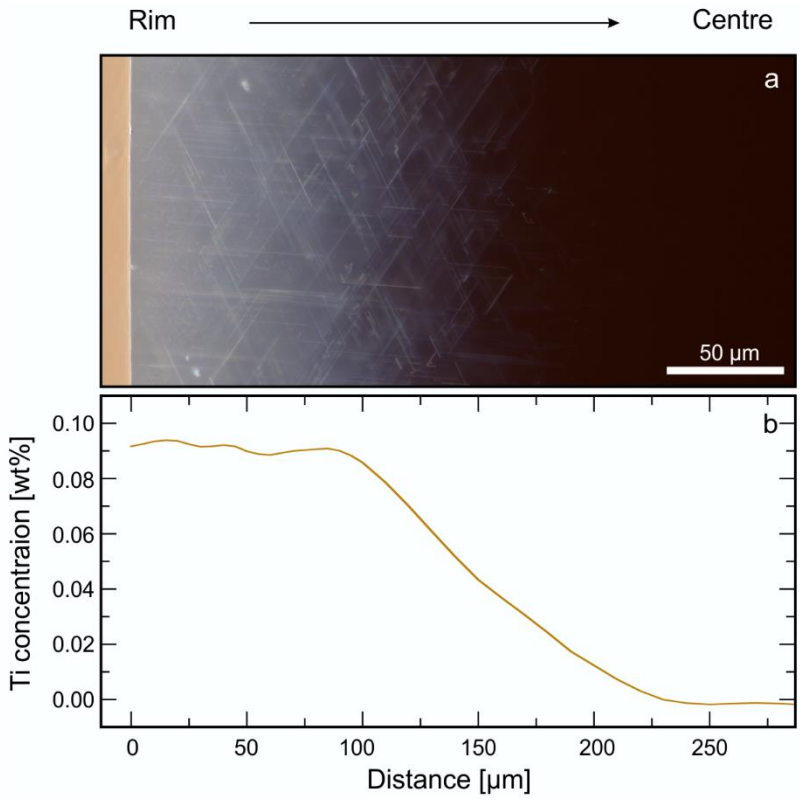

Abb. B 2: (a) Dark-field image (scale = 50 µm): a pale diffusion rim with abundant rutile needles grades into the core, and needle density decreases sharply inward.

(b) EPMA linescan: Ti concentration stays near 0.09 wt% over the first ≈ 100 µm, then falls steadily to < 0.01 wt% beyond ≈ 250 µm.